Growth and Raman Spectra of Single-Crystal Trilayer Graphene with Different Stacking Orientations

Haiming Zhao,[†,§] Yung-Chang Lin,[‡] Chao-Hui Yeh,[§] He Tian,[†] Yu-Chen Chen,[§] Dan Xie,[†] Yi Yang,[†] Kazu Suenaga,[‡] Tian-Ling Ren,[*,†] and Po-Wen Chiu[*,§]

[†]Institute of Microelectronics and Tsinghua National Laboratory for Information Science and Technology (TNList), Tsinghua University, Beijing 100084, China, [‡]National Institute of Advanced Industrial Science and Technology (AIST), Tsukuba 305-8565, Japan, and [§]Department of Electrical Engineering, National Tsing Hua University, Hsinchu 30013, Taiwan

ABSTRACT Understanding the growth mechanism of graphene layers in chemical vapor deposition (CVD) and their corresponding Raman properties is technologically relevant and of importance for the application of graphene in electronic and optoelectronic devices. Here, we report CVD growth of single-crystal trilayer graphene (TLG) grains on Cu and show that lattice defects at the center of each grain persist throughout the growth, indicating that the adlayers share the same nucleation site with the upper layers and these central defects could also act as a carbon pathway for the growth of a new layer. Statistics shows that ABA, 30—30, 30—AB, and AB—30 make up the major stacking orientations in the CVD-grown TLG, with distinctive Raman 2D characteristics. Surprisingly, a high level of lattice defects results whenever a layer with a twist angle of $\theta = 30°$ is found in the multiple stacks of graphene layers.

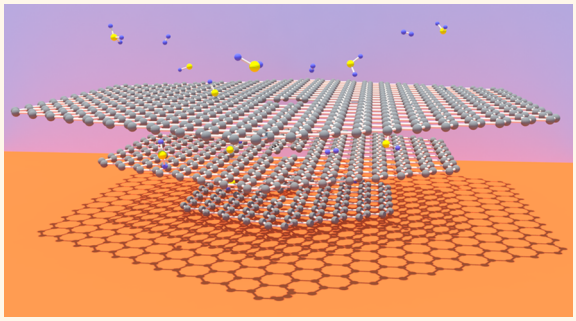

KEYWORDS: trilayer · graphene · stacking · Raman · ALD · TEM

Graphene, a single atomic layer of graphite comprising a planar hexagonal lattice of carbon atoms, has been used in the creation of vertical stacks of homo- and heteroatomic junctions.[1,2] The exotic physical properties of single-layer graphene (SLG) might be changed by placing an adlayer atop the host layer due to the presence of interatomic coupling and producing a variety of interesting properties in the low energy sector of the Dirac spectrum. The gapless band structure in graphene can be lifted as the *A* and *B* sublattices in the unit cell experience different onsite energy; that is, an energy gap can be opened as the inversion symmetry is broken. A well-studied example is bilayer graphene (BLG) with Bernal-type stacking, which exhibits a gate-tunable band gap of up to hundreds of meV, providing appealing opportunities in optoelectronic devices such as infrared light generation, amplification, and detection.[3] This change of the energy spectrum also indicates the breakdown of Klein tunneling, with which Dirac fermions are immune to localization effects observed in ordinary electrons.[4] On the other hand, twisted BLG shows rich physics in its energy spectrum such as twist-angle dependent van Hove singularities,[5] reduction of Fermi velocity,[6] and electric field-tunable particle-hole asymmetry.[7] Placing an additional graphene layer atop the BLG forms a much more complicated trilayer structure. This TLG partially inherits the properties of SLG and BLG, and recent studies have actively explored its diverse electronic structures.[8−16] TLG with typical ABA stacking lacks any appreciable field-induced gap,[17] while TLG with ABC stacking can be gapped at the low energy sector of the spectrum.[18] Analogous to twisted BLG, it has been theoretically shown that the electronic and optical properties of TLG are strongly correlated with the interlayer twist angle,[19,20] providing another unique perspective of understanding interlayer interaction in layered materials.

Micromechanical cleavage of graphite is an early approach that isolates TLG on

* Address correspondence to rentl@tsinghua.edu.cn, pwchiu@ee.nthu.edu.tw.

Received for review August 12, 2014 and accepted October 2, 2014.

Published online October 02, 2014
10.1021/nn5044959

insulating substrates.[12−18] It offers a simple means of obtaining high-quality TLG with ABA or ABC stack and is still the process currently used in most experimental studies. However, a systematic study of the synthesis protocol for different stacking TLG and of their property characterizations is still lacking. The recent development of CVD techniques for graphene growth allows for the scalable production of large-area graphene films for various applications. CVD has been shown to grow high quality single-crystal SLG with lateral dimensions of up to several millimeters by controlling carbon nucleation in a self-limiting reaction.[21,22] Lu *et al.* recently synthesized single-crystal BLG with different twist angles on Cu foils using Ar-diluted CH_4 as the carbon source.[23] Such single-crystal BLG provides a long-range interlayer atomic registry featured by the strong Raman R′ mode, which is both angle and excitation energy dependent. In this paper, the similar CVD technique using Ar-diluted CH_4 is employed to grow single-crystal TLG grains, providing valuable insight into the growth mechanism of multilayer graphene. Raman spectroscopy in combination with transmission electron microscopy (TEM) was used to characterize the as-grown TLG grains, which provides a one-to-one correspondence between the twist angle and Raman properties.

RESULTS AND DISCUSSION

Figure 1 shows the optical micrographs of atmospheric pressure CVD-grown TLG grains with different stacking orientations on an oxidized Si substrate (details about CVD growth are described in the Methods). Each layer has a distinctive color, with a prominent hexagonal shape without apparent interruption by Cu surface imperfections. At a macroscopic scale, the crystallographic edges of the two inner graphene grains are sharp and straight, irrespective of the stacking arrangement. In contrast, some edges of the largest graphene grain become curvy as the grain size is enlarged. Nonetheless, the shapes of these single-crystal grains differ significantly from that of flower-like graphene grains. Crystallographically, we can divide TLG into two BLG with two separate stacking orientations. Then, according to the relationship between two adjacent layers, each TLG grain is labeled as ABA, 30−30, 30−AB, and AB−30, displayed in parts a−d, respectively, of Figure 1.

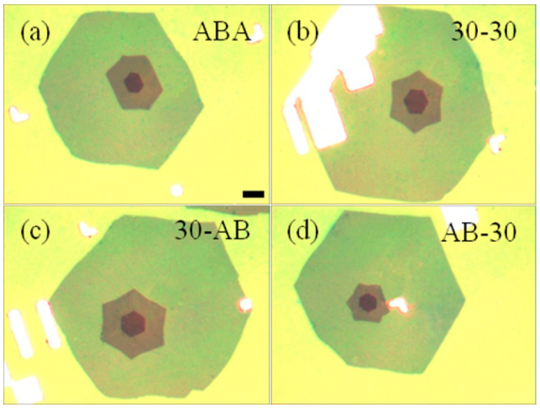

Figure 1. Optical micrographs of as-grown TLG grains after transfer onto SiO_2 (90 nm)/Si substrates. Four different types of stacking arrangements are shown in a−d, respectively. Scale bar: 20 μm.

Atomic layer deposition (ALD) is a thin film growth technique for the deposition of uniform and conformal films with atomic precision and has been widely used in advanced silicon CMOS manufacturing. However, the lack of dangling bonds on the perfect graphene basal plane makes the ALD process problematic.[24] It has been shown that conventional H_2O-based ALD process cannot be used to grow two-dimensional, continuous, and isotropic dielectric films directly on an ideal graphene surface. Nucleation of dielectric embryos is only feasible on graphene edges and defect sites due to the existence of anchor groups.[25−27] This allows for a facile and straightforward means of decorating and visualizing topmost defects in graphene layers. Here, we utilized this technique to deposit Al_2O_3 particles on the as-grown TLG grains to examine the growth mechanism of multilayer graphene.

In our experiment, Al_2O_3 was deposited on as-grown BLG and TLG using 100−150 alternative ALD cycles of trimethylaluminum and H_2O at 200 °C (as described in the Methods). Figure 2a,b shows the SEM images of BLG and TLG grains, respectively, on Cu after growth of Al_2O_3 particles. Two extra satellite second layers are also seen in the BLG grain of Figure 2a. The Al_2O_3 particles are found to grow only spottily on the single-layer region and the center of the bi- and trilayers. Jeon *et al.* showed that the extended long atomic orbital ($3d_{z^2}$) of Cu surface atoms could partially penetrate through the graphene lattice (Figure 2c) and serve as nucleation sites for Al_2O_3 in the ALD process.[28] Thus, it is not surprising to find Al_2O_3 particles growing on the single-layer regions before coarsening into a film. Importantly, the six edges of the smallest hexagon (the third layer) are free of Al_2O_3 particles (Figure 2b), indicating that the third layer is completely isolated from the ALD reactants and appears underneath the upper layers. We attribute the presence of Al_2O_3 particles at the grain centers to the existence of lattice defects. This sort of central defect can be found in all of our BLG and TLG grains and is also revealed in the low-magnification SEM image (Figure S1, Supporting Information). This finding allows us to propose another growth mechanism for multilayer graphene grown on Cu that differs fundamentally from the previous reported mechanism.[29] The early graphene embryos could be composed of defective carbon polygons which persist throughout the growing process. The precursor containing carbons and hydrocarbons could penetrate through those central defects at high

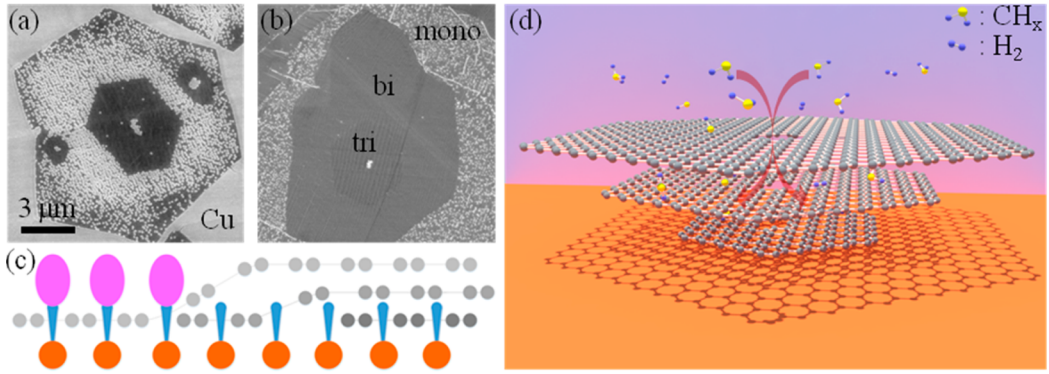

Figure 2. Growth mechanism of CVD-grown TLG on Cu. (a, b) SEM images of BLG and TLG on Cu after growing Al_2O_3 by H_2O-based ALD, respectively. White particles are Al_2O_3. They share the same scale bar. (c) Schematic of Al_2O_3 grown on single-layer graphene. Gray spheres are carbon atoms and orange spheres are Cu atoms. Blue ellipses indicate Cu atomic wave function which could penetrate single-layer graphene and serve as a nucleation center for the Al_2O_3 (purple ellipses). (d) Growth schematic for TLG. CH_x could diffuse through the defect hole of the upper layer graphene, rather than sides, to nucleate on the Cu surface.

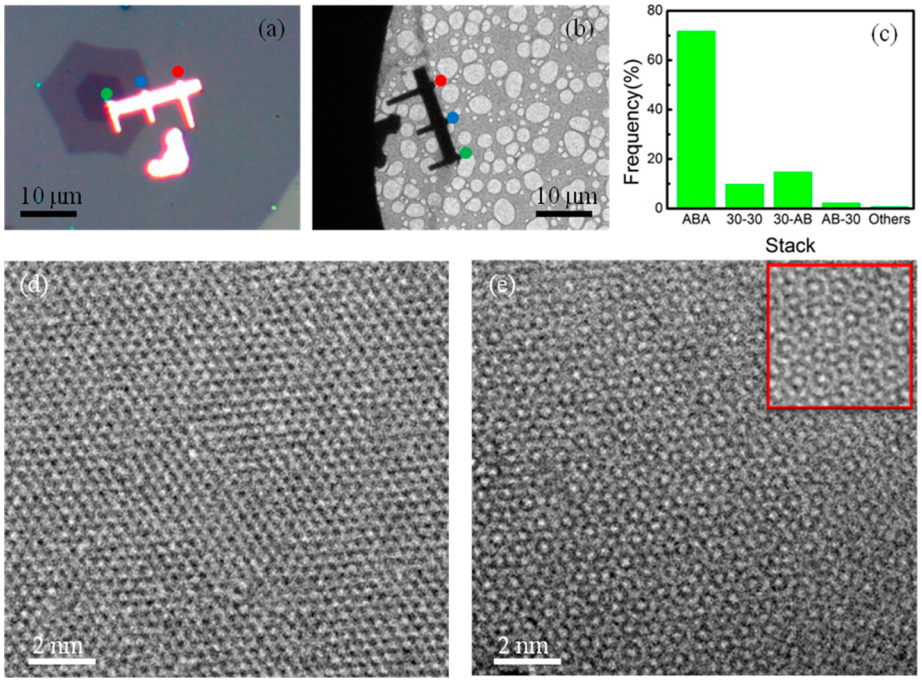

Figure 3. One-to-one Raman and TEM characterization. (a, b) Optical micrograph of the marker/graphene on SiO_2/Si substrate and low magnification TEM image of the same structure transferred onto a Cu grid, respectively. The red (monolayer), blue (bilayer), and green (trilayer) points represent the corresponding locations for Raman and TEM. (c) Stacking frequency of as-grown TLG grains. Excluding 30°, rare other twist angles were found. (d, e) HR-TEM images of ABA and 30−30 TLG grains, respectively. ABA-stacked TLG shows the triangular pattern characteristic, while 30−30 stacked TLG looks similar to 30°-twisted BLG (as shown in the inset). No moiré pattern was found in 30−30 TLG because the 30° twist angle is not commensurate.

temperatures, nucleating the adlayer underneath the upper layers. The adlayer extends from the center over time as long as carbon source is provided. Figure 2d schematically illustrates this mechanism. This picture is basically consistent with the ^{13}C-labeled growth reported by Li *et al.* and Fang *et al.*[29,30] However, these previous studies failed to reveal the growth from the center, which is, as a matter of practice, vital to the rational tailoring of the stacking orientation during growth of multilayer graphene.

Selected area electron diffraction (SAED) in TEM was used to reveal the relative stacking orientations of TLG characterized by Raman spectroscopy. Figure 3a,b shows the one-to-one correlation for Raman and TEM characterization. The detailed fabrication procedure is described in Figure S2 (Supporting Information). To gain insight into the distribution of stacking arrangements, more than 230 TLG samples were inspected. Figure 3c presents a statistical analysis of the stacking frequency, showing that 70% of the as-grown TLG are ABA stack, which is energetically most favorable in nature. Based on the limited statistics, no ABC stack is explicitly identified. Only about 10%, 15%, and 3% are found, respectively, for the 30−30, 30−AB, and AB−30 stacks. It is also worth noting that our previous study shown that non-30° twisted grains take up ~25%

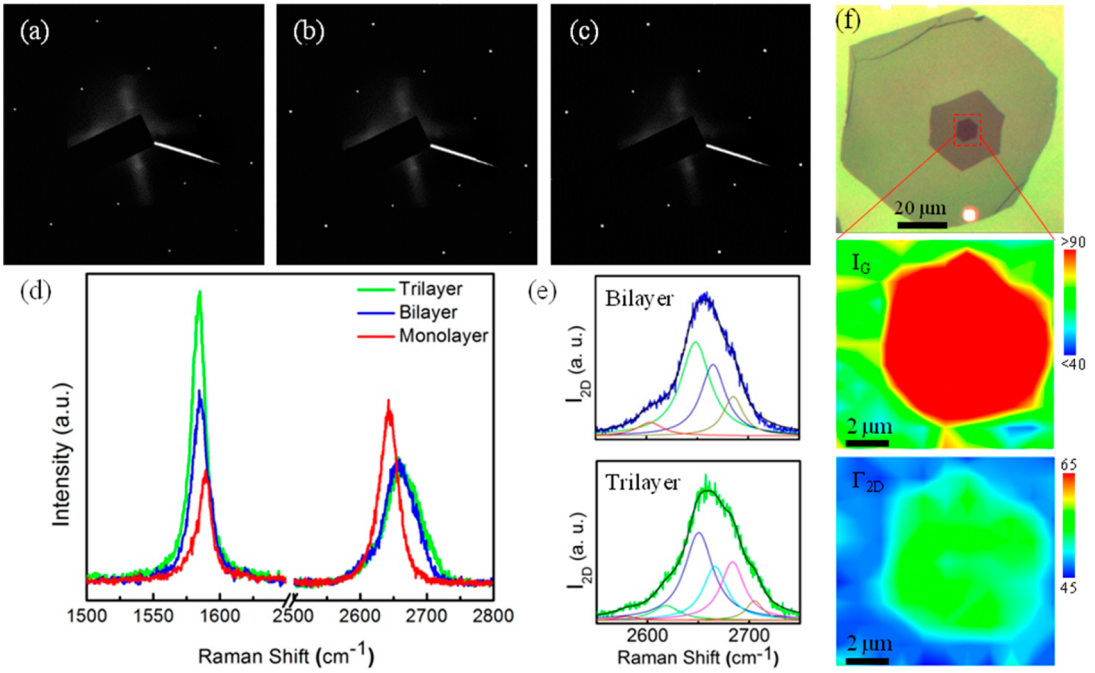

Figure 4. Raman spectra and TEM of an ABA-stacked TLG grain. (a−c) SAED patterns of mono-, bi-, and trilayer regions, respectively. (d) Corresponding G and 2D peaks of the same TLG grain under 633 nm laser excitation. (e) Fitting for 2D peaks of bi- and trilayer regions, indicating four and six Lorentzians are needed for bi- and trilayers, respectively. The black line is the sum of subpeaks. (f) Raman mapping with step size of 1 μm under 532 nm laser excitation. The upper panel is the optical image (only the central trilayer region with surrounded bilayer region was mapped as shown in the red dash rectangle), while the middle and bottom panels are G peak intensity and fwhm of the 2D peak, respectively.

of twisted BLG[23] but are rarely found (<1%) in TLG. The percentage of interlayer twist drops dramatically as both the number of stacks and grain size increase. This implies that twisted orientation is energetically unfavorable and the grain might reorient at high temperatures as the growth duration is prolonged.

We performed Raman measurements using a scanning confocal setup with laser wavelengths of 633, 532, and 488 nm. To avoid heating and damage, the laser spot was focused to a diffraction-limited size with a power below 2 mW. The Raman spectra of CVD-grown TLG with different stacking arrangements show a rich variation in peak intensities and shapes. Parts a−c, respectively, of Figure 4 show the SAED patterns of mono-, bi-, and trilayer regions of an ABA-stacked TLG grain. A high-resolution TEM (HR-TEM) image is shown in Figure 3d. As expected, the diffraction pattern of each layer exhibits a typical 6-fold symmetry and is mutually overlapping, indicating a single-crystal structure with no relative twist and no gliding-induced transition of domain orientation. Figure 4d shows the corresponding Raman spectra for the mono- (red), bi- (blue), and tri- (green) layer regions. Two intense Raman peaks, located at ~1588 and ~2650 cm^{-1}, respectively, represent the G and 2D modes. The G peak stems from the in-plane vibration of sp^2 carbon atoms, with an intensity proportional to the stacking numbers (<10 layers) due to the constructive interference and multireflections of light.[31] This is evident in Figure 4d, where the G peak intensity increases linearly with the number of layers, *i.e.*, I_G(BLG) ≈ 2I_G(SLG) and I_G(TLG) ≈ 3I_G(SLG). Interestingly, the G peak frequency is red-shifted, and the full width at half-maximum (fwhm) increases in both the bilayer and trilayer regions (summarized in Table S1, Supporting Information). These phenomena also apply to other TLG grains, irrespective of the stacking orientations. These effects can be understood in the framework presented by Berciaud *et al.*,[32] in which the suspended SLG shows a clear redshift and broadened fwhm of the G peak in comparison to the supported SLG, owing to the substrate-induced inhomogeneous doping. The progressive weakening of the substrate effect to the upper layers could be the primary cause of the G peak redshift and broadening. For the 2D peak, the SLG profile is symmetric and can be well described by a single Lorentzian with I_{2D} ~1.5I_G, as shown in Figure S3 (Supporting Information). For the Bernal-stacked bilayer region, the energy band splits into two parabolic subbands due to the π electron overlap and strong interlayer interaction. Four different Raman scattering pathways with slightly different frequencies are then expected. As a result, the Raman spectra of the Bernal-stacked bilayer region can be fitted with four Lorentzians (upper panel in Figure 4e),[33] without perturbation stemming from the presence of the third layer. Likewise, to correctly identify the 2D line shape for the ABA-stacked trilayer, one should model the double-resonance (DR) Raman process with considering 15 different transitions.[34] However, the energy

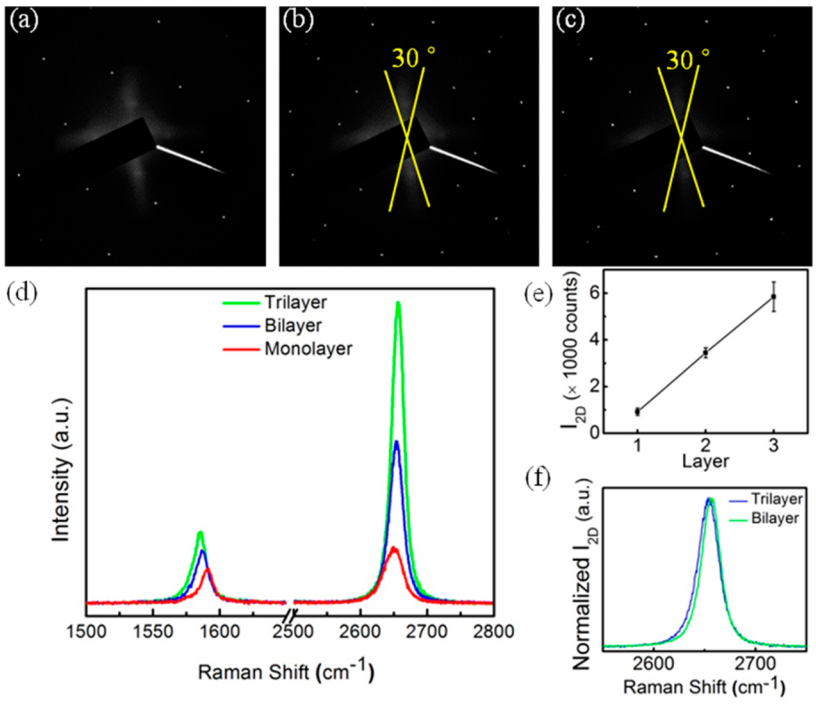

Figure 5. Raman spectra and TEM of a 30−30 stacked TLG grain. (a−c) SAED patterns of mono-, bi-, and trilayer regions, respectively. (d) Corresponding G and 2D peaks of the same TLG grain under 633 nm laser excitation. (e) 2D peak intensity as a function of number of 30° twisted layers. (f) Normalized 2D peak intensity of bi- and trilayer regions.

separations of these different scattering processes turn out to be so close to each other that the line shape can be properly identified by 6 subpeaks,[14,15] as shown in the bottom panel of Figure 4e. As previously reported, ABC-stacked TLG shows a larger 2D peak width (Γ_{2D}) than the ABA-stacked TLG. This spectral difference can be used to distinguish between ABC and ABA stacking.[14,15] Therefore, we mapped the central trilayer region, as shown in Figure 4f. The clear contrast of the I_G map outlines the shape of the trilayer region where the Γ_{2D} is rather uniform (with variation less than 4 cm^{-1}), indicating a single stacking orientation in the TLG. Further comparison with the Raman spectra of ABA and ABC allowed us to identify this TLG as ABA.[14,15]

Parts a−c, respectively, of Figure 5 present the SAED patterns of mono-, bi-, and trilayer regions of a 30−30 stacked TLG grain. Its HR-TEM image is shown in Figure 3e. The SAED patterns of bi- and trilayer regions are intuitively identical, making it difficult to differentiate between 30−30 and 30−AB stacks based on a comparison of the SAED patterns alone. A subtle difference can be found in the intensity of the diffraction spots, providing a means of identification. Their corresponding Raman spectra are presented in Figure 5d. The G peaks show intensity, position, and profile properties similar to those of ABA-stacked TLG. On the contrary, the 2D peak intensity and width of 30−30 stacked TLG are distinct from those of ABA-stacked TLG. For 30−30 stacked TLG, the 2D peak intensity increases linearly with the number of layers (Figure 5e), namely, $I_{2D}(BLG) \approx 3.8 I_{2D}(SLG)$ and $I_{2D}(TLG) \approx 6.3 I_{2D}(SLG)$. Previous studies have shown that the 2D peak intensities of twisted BLG increases monotonically with the twist angle, and the $I_{2D}(BLG)/I_{2D}(SLG)$ ratio reaches a maximum value of 2.5−3.0 in 30°-twisted BLG.[35,36] In light of this result, the 30−30 stacked TLG can be rationally regarded as a conjunction of two separate 30°-twisted BLG systems. If we normalize the 2D peak intensity of bi- and trilayer regions to unity, this argument is also supported by the fact that the normalized 2D peak of TLG is nearly identical with that of BLG (Figure 5f). Inspecting the mean value of Γ_{2D}, we found that the SLG takes 31 ± 1 cm^{-1}, while both the BLG and TLG share the close value of 22 ± 2 cm^{-1}. Meanwhile, 2D line shapes of both BLG and TLG can be fitted by a single Lorentzian (Figure S4, Supporting Information). What's more, an appreciable upshift of the 2D peak position of ~13 cm^{-1} was also observed when moving from the SLG to the TLG region. This result is in accord with Forster's work,[37] in which the 2D peak upshift is attributed to the partial removal of the Kohn-anomaly in the phonon dispersion near the K point due to increased screening in the multilayer graphene.

Parts a and c, respectively, of Figure 6 present the Raman G and 2D peaks of 30−AB and AB−30 TLG grains. Their corresponding SEAD patterns are shown in Figure S5 (Supporting Information). Apparently, the 2D peak of the bilayer region of 30−AB can be well described by a single Lorentzian, while that of AB−30 is fitted by four Lorentzians. Since TLG can be regarded as the coupling of two BLG systems (AB−BLG and

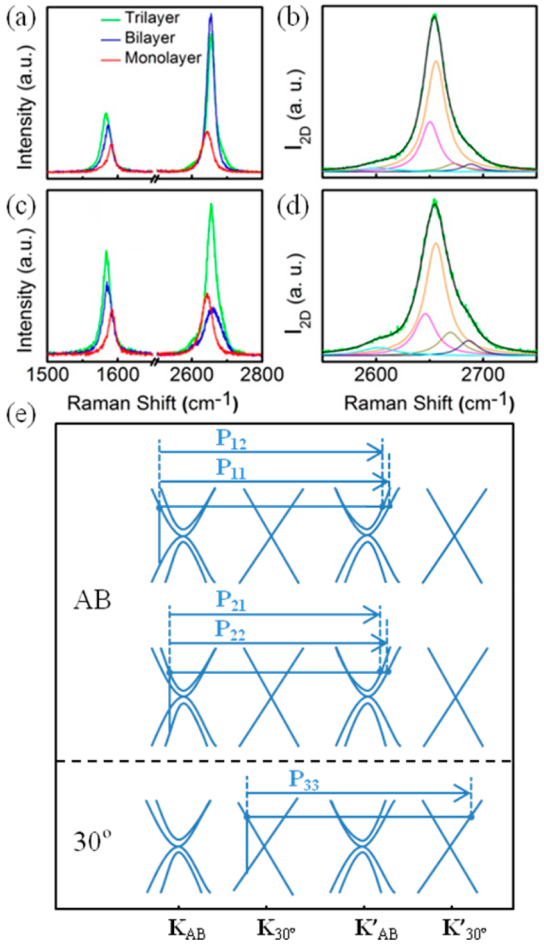

Figure 6. Raman spectra of 30−AB and AB−30 stacked TLG grains. (a, c) Raman spectra of mono-, bi-, and trilayer regions in 30−AB and AB−30 stacked TLG grains under 633 nm laser excitation, respectively. (b, d) Fittings for 2D peaks of trilayer regions in 30−AB and AB−30 TLG grains, respectively. The black line is the sum of subpeaks. (e) Suggested DR process of the five Lorentzians. P_{ij} (i, j = 1, 2) stands for the DR process of AB stacked bilayer while P_{33} is the DR process of the 30° twisted graphene layer.

30°-twisted BLG in this case), the 2D profile of the trilayer region is then composed of the 2D profiles of two separate BLGs. This is evident in Figure 6b ,d, where the 2D peaks of the trilayer region in both the 30−AB and AB−30 TLG can be well described by five Lorentzian subpeaks.

An interesting Raman feature was observed whenever a 30° twist exists. We found that the 30° twist causes noticeable defects uniformly distributed in the stacks. Figure 7 shows a close-up of the Raman properties of the above four different TLG grains in the frequency range between 1200 and 1500 cm^{-1} where the prominent D and R modes are located. The D and R peaks are both caused by an intervalley DR process. Similar to the disorder-induced D peak, the R peak, which appears only at large twist angles, involves two scattering steps: elastic electron scattering by the static potential of the superlattice and inelastic electron scattering by the iTO phonon around the K point.[23,38] This similar Raman scattering origin yields an R peak frequency nearly overlapping with that of the D peak. Fortunately, the D peak is energy dispersive, while the R peak is not. That is, the D peak frequency increases with excitation energy, thus allowing for differentiation. In Figure 7, the black dashed rectangle frames the D peak which exhibits an energy dispersion of ~50 cm^{-1}/eV, consistent with previous reports.[39] The adjacent peak, which is nondispersive and centered at ~1379 cm^{-1}, is identified as the twist-induced R peak. It is visible in all the 30−30, 30−AB, and AB−30 TLG grains, as marked by the pink dashed line in Figure 7. Note that no R peak was found under 633 nm excitation owing to a lack of sufficient energy to trigger this Raman mode.[38] In sharp contrast to the TLG containing a 30°-twisted layer, no detectable D peak was found in the ABA stacked TLG. The D to G peak intensity ratio in ABA stacked TLG is $I_D/I_G \approx 0$, increasing to $I_D/I_G \approx$ 0.01−0.05 in the 30−30, 30−AB, and AB−30 TLG grains. We exclude the origin of the defects from postgrowth processing like wet transfer. This is evident in the absence of D peak in the single-layer region of the 30−30, 30−AB, and AB−30 TLG. Notably, the intensity of this twist-induced D peak increases with the number of twisted layers. For example, 30−30 TLG exhibits an enhanced D peak intensity when compared with 30−AB TLG. The origin of the twist-induced peak enhancement is currently unclear and will be an interesting topic for future studies.

CONCLUSIONS

In conclusion, we have synthesized large hexagonal single-crystal TLG grains on Cu using atmospheric pressure CVD, with ABA, 30−30, 30−AB, and AB−30 being the major stacking configurations. Two TLG grains with small twist angles are shown in Figures S6 and S7 (Supporting Information). Through the deposition of Al_2O_3 particles on as-grown TLG grains using H_2O-based ALD, we show that the adlayers graphene nucleate from defect sites of the host layer and grow underneath. Also, the as-grown TLG grains are of high crystalline quality, as revealed by the low I_D/I_G. A systematic study of stacking-dependent TLG Raman characteristics is provided, paving the way for optical characterizations and potential applications in electronic and optoelectronic devices which require versatile energy spectra.

METHODS

Graphene Synthesis. Large hexagonal single-crystal TLG grains were grown by atmospheric pressure CVD of Ar-diluted methane (80 ppm) on 10 μm thickness polycrystalline Cu foils. Prior to growth, the Cu foils were cleaned using acetone and IPA, followed by etching in acetic acid for 30 min to remove

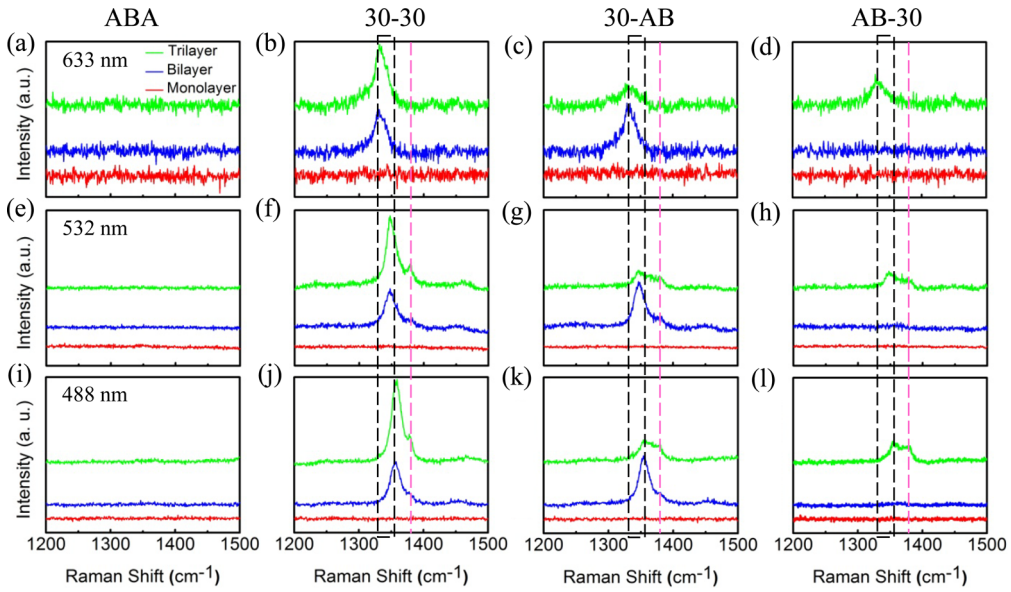

Figure 7. D and R peaks of four different stacking TLG. Panels a−d, e−h, and i−l are measured under 633, 532, and 488 nm laser excitations, respectively. In all panels, red, blue, and green lines represent the Raman spectra of mono-, bi-, and trilayer regions, respectively. D peaks are marked with black rectangles, while R peaks are shown with pink lines. The Raman spectra are offset vertically for clarity.

surface oxides. The Cu foils were then mounted in the CVD chamber, and the furnace was heated to 1050 °C over 30 min with constant flows of 300 sccm Ar and 15 sccm H_2. After a temperature of 1050 °C was reached, the Cu foils were annealed for 150 min without changing the gas flow. For graphene growth, 170 sccm methane mixed with the flows of 130 sccm Ar and of 18 sccm H_2 was fed into the reaction chamber for 90 min to form TLG. Following the growth, the Cu foils were moved to the cooling zone under the protection of Ar and H_2.

ALD Al_2O_3. Immediately following CVD growth, the TLG sheets on the Cu foils were moved into a commercial ALD reactor (Savannah S100, Cambridge Nano Tech, Inc.) to prevent contamination by molecules in the air. The chamber was pumped down to a pressure of 0.3 Torr with N_2 purging of 20 sccm. It took about 1 h to heat the chamber to the growth temperature (200 °C) from room temperature. Next, Al_2O_3 films in 100−150 cycles were deposited on top of the graphene using trimethylaluminum (TMA) and water (H_2O) as reactants. For one ALD cycle, the pulse time of TMA and H_2O was held constant at 5s. The deposited Al_2O_3 was characterized by SEM.

Raman Spectroscopy. A high-resolution confocal Raman spectrometer (LabRaman 800, Horiba Jobin Yvon) equipped with a motorized sample stage was used to acquire the Raman spectra and spatial mapping. A 100× objective lens was used to provide a diffraction-limited spot size. Laser excitations of 633, 532, and 488 nm were used with power levels set below 1−2 mW to avoid heating or damaging the sample.

Transmission Electron Microscopy. A field emission TEM JEM-2010F (JEOL) equipped with a CEOS postspecimen spherical aberration corrector (Cs corrector) was operated at 120 kV for the TEM observations. A Gatan 894 CCD camera was used to digitally record the SAED patterns and HR-TEM images. A sequence of HR-TEM images (10 frames) was recorded, each with an exposure time of 1 s. After drift compensation, some frames can be superimposed to increase the signal-to-noise (SN) ratio for display.

Conflict of Interest: The authors declare no competing financial interest.

Acknowledgment. T.-L.R. acknowledges the project support by the National Natural Science Foundation (61025021, 61434001) and National Key Project of Science and Technology (2011ZX02403-002) of China. P.-W.C. appreciates the project support by National Tsing Hua University and the Taiwan Ministry of Science and Technology: MOST 103-2628-M-007-004-MY3; MOST 103-2119-M-007-008-MY3; and MOST 102-2633-M-007-002-(P.-W. C.).

Supporting Information Available: Additional Raman and TEM characterizations. This material is available free of charge *via* the Internet at http://pubs.acs.org.

REFERENCES AND NOTES

1. Geim, A. K.; Grigorieva, I. V. Van Der Waals Heterostructures. *Nature* **2013**, *499*, 419–425.
2. Kim, C. O.; Kim, S.; Shin, D. H.; Kang, S. S.; Kim, J. M.; Jang, C. W.; Joo, S. S.; Lee, J. S.; Kim, J. H.; Choi, S. H.; *et al.* High Photoresponsivity in An All-Graphene P-N Vertical Junction Photodetector. *Nat. Commun.* **2014**, *5*, 3249.
3. Zhang, Y. B.; Tang, T. T.; Girit, C.; Hao, Z.; Martin, M. C.; Zettl, A.; Crommie, M. F.; Shen, Y. R.; Wang, F. Direct Observation of A Widely Tunable Bandgap in Bilayer Graphene. *Nature* **2009**, *459*, 820–823.
4. Katsnelson, M. I.; Novoselov, K. S.; Geim, A. K. Chiral Tunnelling and The Klein Paradox in Graphene. *Nat. Phys.* **2006**, *2*, 620–625.
5. Yan, W.; Liu, M. X.; Dou, R. F.; Meng, L.; Feng, L.; Chu, Z. D.; Zhang, Y. F.; Liu, Z. F.; Nie, J. C.; He, L. Angle-Dependent Van Hove Singularities in A Slightly Twisted Graphene Bilayer. *Phys. Rev. Lett.* **2012**, *109*, 126801.
6. Luican, A.; Li, G. H.; Reina, A.; Kong, J.; Nair, R. R.; Novoselov, K. S.; Geim, A. K.; Andrei, E. Y. Single-Layer Behavior and Its Breakdown in Twisted Graphene Layers. *Phys. Rev. Lett.* **2011**, *106*, 126802.
7. Yeh, C. H.; Lin, Y. C.; Chen, Y. C.; Lu, C. C.; Liu, Z.; Suenaga, K.; Chiu, P. W. Gating Electron-Hole Asymmetry in Twisted Bilayer Graphene. *ACS Nano* **2014**, *8*, 6962–6969.
8. Guinea, F.; Castro Neto, A. H.; Peres, N. M. R. Electronic States and Landau Levels in Graphene Stacks. *Phys. Rev. B* **2006**, *73*, 245426.
9. Partoens, B.; Peeters, F. M. From Graphene to Graphite: Electronic Structure around The K Point. *Phys. Rev. B* **2006**, *74*, 075404.
10. Partoens, B.; Peeters, F. M. Normal and Dirac Fermions in Graphene Multilayers: Tight-Binding Description of The Electronic Structure. *Phys. Rev. B* **2007**, *75*, 193402.
11. Aoki, M.; Amawashi, H. Dependence of Band Structures on Stacking and Field in Layered Graphene. *Solid State Commun.* **2007**, *142*, 123–127.

12. Bao, W.; Jing, L.; Velasco, J.; Lee, Y.; Liu, G.; Tran, D.; Standley, B.; Aykol, M.; Cronin, S. B.; Smirnov, D.; *et al.* Stacking-Dependent Band Gap and Quantum Transport in Trilayer Graphene. *Nat. Phys.* **2011**, *7*, 948–952.
13. Zhang, L. Y.; Zhang, Y.; Camacho, J.; Khodas, M.; Zaliznyak, I. The Experimental Observation of Quantum Hall Effect of l−3 Chiral Quasiparticles in Trilayer Graphene. *Nat. Phys.* **2011**, *7*, 953–957.
14. Lui, C. H.; Li, Z. Q.; Chen, Z. Y.; Klimov, P. V.; Brus, L. E.; Heinz, T. F. Imaging Stacking Order in Few-Layer Graphene. *Nano Lett.* **2011**, *11*, 164–169.
15. Cong, C. X.; Yu, T.; Sato, K.; Shang, J. Z.; Saito, R.; Dresselhaus, G. F.; Dresselhaus, M. S. Raman Characterization of ABA- and ABC-Stacked Trilayer Graphene. *ACS Nano* **2011**, *5*, 8760–8768.
16. Campos, L. C.; Young, A. F.; Surakitbovorn, K.; Watanabe, K.; Taniguchi, T.; Jarillo-Herrero, P. Quantum and Classical Confinement of Resonant States in A Trilayer Graphene Fabry-Perot Interferometer. *Nat. Commun.* **2012**, *3*, 1239.
17. Craciun, M. F.; Russo, S.; Yamamoto, M.; Oostinga, J. B.; Morpurgo, A. F.; Tarucha, S. Trilayer Graphene Is A Semimetal with A Gate-Tunable Band Overlap. *Nat. Nanotechnol.* **2009**, *4*, 383–388.
18. Lui, C. H.; Li, Z. Q.; Mak, K. F.; Cappelluti, E.; Heinz, T. F. Observation of An Electrically Tunable Band Gap in Trilayer Graphene. *Nat. Phys.* **2011**, *7*, 944–947.
19. Morell, E. S.; Pacheco, M.; Chico, L.; Brey, L. Electronic Properties of Twisted Trilayer Graphene. *Phys. Rev. B* **2013**, *87*, 125414.
20. Correa, J. D.; Pacheco, M.; Morell, E. S. Optical Absorption Spectrum of Rotated Trilayer Graphene. *J. Mater. Sci.* **2014**, *49*, 642–647.
21. Yan, Z.; Lin, J.; Peng, Z. W.; Sun, Z. Z.; Zhu, Y.; Li, L.; Xiang, C. S.; Samuel, E. L.; Kittrell, C.; Tour, J. M. Toward The Synthesis of Wafer-Scale Single-Crystal Graphene on Copper Foils. *ACS Nano* **2012**, *6*, 9110–9117.
22. Mohsin, A.; Liu, L.; Liu, P. Z.; Deng, W.; Ivanov, I. N.; Li, G. L.; Dyck, O. E.; Duscher, G.; Dunlap, J. R.; Xiao, K.; *et al.* Synthesis of Millimeter-Size Hexagon-Shaped Graphene Single Crystals on Resolidified Copper. *ACS Nano* **2013**, *7*, 8924–8931.
23. Lu, C. C.; Lin, Y. C.; Liu, Z.; Yeh, C. H.; Suenaga, K.; Chiu, P. W. Twisting Bilayer Graphene Superlattices. *ACS Nano* **2013**, *7*, 2587–2594.
24. George, S. M. Atomic Layer Deposition: An Overview. *Chem. Rev.* **2010**, *110*, 111–131.
25. Lee, B. K.; Park, S. Y.; Kim, H. C.; Cho, K.; Vogel, E. M.; Kim, M. J.; Wallace, R. M.; Kim, J. Y. Conformal Al_2O_3 Dielectric Layer Deposited by Atomic Layer Deposition for Graphene-Based Nanoelectronics. *Appl. Phys. Lett.* **2008**, *92*, 203102.
26. Wang, X. R.; Tabakman, S. M.; Dai, H. J. Atomic Layer Deposition of Metal Oxides on Pristine and Functionalized Graphene. *J. Am. Chem. Soc.* **2008**, *130*, 8152–8153.
27. Xuan, Y.; Wu, Y. Q.; Shen, T.; Qi, M.; Capano, M. A.; Cooper, J. A.; Ye, P. D. Atomic-Layer-Deposited Nanostructures for Graphene-Based Nanoelectronics. *Appl. Phys. Lett.* **2008**, *92*, 013101.
28. Jeon, I.; Yang, H.; Lee, S. H.; Heo, J.; Seo, D. H.; Shin, J.; Chung, U. I.; Kim, Z. G.; Chung, H. J.; Seo, S. Passivation of Metal Surface States: Microscopic Origin for Uniform Monolayer Graphene by Low Temperature Chemical Vapor Deposition. *ACS Nano* **2011**, *5*, 1915–1920.
29. Li, Q. Y.; Chou, H.; Zhong, J. H.; Liu, J. Y.; Dolocan, A.; Zhang, J. Y.; Zhou, Y. H.; Ruoff, R. S.; Chen, S. S.; Cai, W. W. Growth of Adlayer Graphene on Cu Studied by Carbon Isotope Labeling. *Nano Lett.* **2013**, *13*, 486–490.
30. Fang, W.; Hsu, A. L.; Caudillo, R.; Song, Y.; Birdwell, A. G.; Zakar, E.; Kalbac, M.; Dubey, M.; Palacios, T.; Dresselhaus, M. S.; *et al.* Rapid Identification of Stacking Orientation in Isotopically Labeled Chemical-Vapor Grown Bilayer Graphene by Raman Spectroscopy. *Nano Lett.* **2013**, *13*, 1541–1548.
31. Wang, Y. Y.; Ni, Z. H.; Shen, Z. X.; Wang, H. M.; Wu, Y. H. Interference Enhancement of Raman Signal of Graphene. *Appl. Phys. Lett.* **2008**, *92*, 043121.
32. Berciaud, S.; Ryu, S.; Brus, L. E.; Heinz, T. F. Probing The Intrinsic Properties of Exfoliated Graphene: Raman Spectroscopy of Free-Standing Monolayers. *Nano Lett.* **2009**, *9*, 346–352.
33. Ferrari, A. C.; Meyer, J. C.; Scardaci, V.; Casiraghi, C.; Lazzeri, M.; Mauri, F.; Piscanec, S.; Jiang, D.; Novoselov, K. S.; Roth, S.; *et al.* Raman Spectrum of Graphene and Graphene Layers. *Phys. Rev. Lett.* **2006**, *97*, 187401.
34. Malard, L. M.; Guimaraes, M. H. D.; Mafra, D. L.; Mazzoni, M. S. C.; Jorio, A. Group-Theory Analysis of Electrons and Phonons in N-Layer Graphene Systems. *Phys. Rev. B* **2009**, *79*, 125426.
35. Havener, R. W.; Zhuang, H. L.; Brown, L.; Hennig, R. G.; Park, J. Angle-Resolved Raman Imaging of Interlayer Rotations and Interactions in Twisted Bilayer Graphene. *Nano Lett.* **2012**, *12*, 3162–3167.
36. Kim, K.; Coh, S.; Tan, L. Z.; Regan, W.; Yuk, J. M.; Chatterjee, E.; Crommie, M. F.; Cohen, M. L.; Louie, S. G.; Zettl, A. Raman Spectroscopy Study of Rotated Double-Layer Graphene: Misorientation-Angle Dependence of Electronic Structure. *Phys. Rev. Lett.* **2012**, *108*, 246103.
37. Forster, F.; Molina-Sanchez, A.; Engels, S.; Epping, A.; Watanabe, K.; Taniguchi, T.; Wirtz, L.; Stampfer, C. Dielectric Screening of The Kohn Anomaly of Graphene on Hexagonal Boron Nitride. *Phys. Rev. B* **2013**, *88*, 085419.
38. Carozo, V.; Almeida, C. M.; Ferreira, E. H. M.; Cancado, L. G.; Achete, C. A.; Jorio, A. Raman Signature of Graphene Superlattices. *Nano Lett.* **2011**, *11*, 4527–4534.
39. Pimenta, M. A.; Dresselhaus, G.; Dresselhaus, M. S.; Cancado, L. G.; Jorio, A.; Saito, R. Studying Disorder in Graphite-Based Systems by Raman Spectroscopy. *Phys. Chem. Chem. Phys.* **2007**, *9*, 1276–1291.